nature communications

Article

https://doi.org/10.1038/s41467-025-59933-6

Interlayer-bonded Ni/MoO_2 electrocatalyst for efficient hydrogen evolution reaction with stability over 6000 h at 1000 mA cm^{-2}

Received: 3 January 2025

Accepted: 5 May 2025

Published online: 28 May 2025

Check for updates

Anrui Dong[1,2,4], Gaoxin Lin[1,2,4], Zhiheng Li[1,2], Wen Wu[1,2], Xing Cao[1,2], Wenlong Li[1,2], Linqin Wang[1,2], Yilong Zhao[1,2], Dexin Chen[1,2] & Licheng Sun[1,2,3]

The mechanical stability of the catalytic electrodes used for hydrogen evolution reactions (HER) is crucial for their industrial applications in anion exchange membrane water electrolysis (AEM-WE). This study develops a corrosion strategy to construct a self-supported electrocatalyst (Int-Ni/MoO_2) with high mechanical stability by anchoring the Ni/MoO_2 catalytic layer with a dense interlayer of MoO_2 nanoparticles. The Int-Ni/MoO_2 exhibits a strengthened homostructural interface between the interlayer and catalytic layer, preventing the detachment of the catalyst during ultrasonic treatment. The blade-shaped catalytic layer reduces bubble shock and potential fluctuations at high current densities up to −6000 mA cm^{-2}. As a result, the Int-Ni/MoO_2 electrode exhibits a low overpotential of 73.2 ± 14.2 mV and long-term stability for 6000 h at −1000 mA cm^{-2} in a 1 M KOH solution. The Int-Ni/MoO_2 assembled AEM-WE device demonstrates long-term stability at 1000 mA cm^{-2} for 1000 h with a very low degradation rate of 3.96 μV h^{-1}.

Ampere-scale anion exchange membrane water electrolysis (AEM-WE) is crucial for achieving a sustainable hydrogen economy[1–4]. The hydrogen evolution reaction (HER) at the cathode, which yields twice as much gas as the oxygen evolution reaction at the anode, is still limited by the lack of efficient and stable electrocatalysts under harsh reaction conditions[5,6]. As the current is increased from the milliampere to ampere scale, inhibited electron transfer at the liquid–solid interface and limited mass transfer at the gas–liquid–solid interface result in high overpotentials for the HER[7–10]. Moreover, the generation of massive bubbles causes uneven distributions of local stress and interfacial adhesion force, which may detach the catalyst layer from the electrode[8,11,12]. The above issues pose significant challenges in designing electrodes with long-term stability.

Polystyrene-based ionomers with high ion conductivities can reduce the overpotentials at high current densities in AEM-WE[13,14], however, these binders cannot provide a strong adhesion force for catalysts during a fast HER, highlighting the need for the development of self-supported catalytic electrodes with enhanced catalyst-substrate interactions. Recent studies suggest that electrodes based on transition-metal oxides, sulfides, or phosphides, through the in situ growth of a catalytic layer on the substrate, have demonstrated low degradation for over 100 h at high current densities (≥ 1000 mA cm^{-2})[15–20]. However, an ultrastable electrode capable of maintaining an ampere-scale current density for several thousand hours is still lacking because of weak electrostatic adsorption, mechanical interlocking, or intermolecular attractions at the heterostructure interface[6,21]. Therefore, reinforcing the interactions between the substrate and catalyst and mitigating the impact of bubbles on the interface remain major challenges in achieving long-term stability.

Herein, we developed a corrosion strategy to construct a self-supported electrocatalyst (Int-Ni/MoO_2) with high mechanical stability by anchoring a blade-shaped catalytic layer (Ni/MoO_2) onto a dense

[1]Center of Artificial Photosynthesis for Solar Fuels and Department of Chemistry, School of Science and Research Center for Industries of the Future, Westlake University, 600 Dunyu Road, Hangzhou 310030 Zhejiang Province, China. [2]Institute of Natural Sciences, Westlake Institute for Advanced Study, 18 Shilongshan Road, Hangzhou 310024 Zhejiang, China. [3]Division of Solar Energy Conversion and Catalysis at Westlake University, Zhejiang Baima Lake Laboratory Co., Ltd., Hangzhou 310000 Zhejiang Province, China. [4]These authors contributed equally: Anrui Dong, Gaoxin Lin. e-mail: sunlicheng@westlake.edu.cn

interlayer (MoO_2) (Fig. 1a). The interlayer transfers the bubble shock from the heterostructural interface (between the substrate and the catalytic layer) to the homostructural interface (between the interlayer and the catalytic layer), enhancing the catalytic activity and stability in ampere-scale HER. In a 1 M KOH solution, Int-Ni/MoO_2 exhibits an overpotential of 73.2 ± 14.2 mV at −1000 mA cm^{-2}, significantly lower than that of Pt/C (243.0 ± 2.9 mV). Furthermore, it demonstrates good stability, operating for >6000 h without any discernible degradation. The Int-Ni/MoO_2-assembled noble metal-free AEM-WE device achieves a high current density of 7570 mA cm^{-2} at 2.0 V and a long-term stability of 1000 h at 1000 mA cm^{-2}.

Results and discussion

Int-Ni/MoO_2 was synthesised via a corrosion strategy by soaking the nickel foam (NF) in an $(NH_4)_6Mo_7O_{24}$ solution with polyvinylpyrrolidone (PVP) as the ligand (Fig. S1 and S2). A blade-shaped structure was generated following the subsequent hydrothermal treatment (Fig. S3). X-ray diffraction (XRD) patterns confirmed that the heterostructure comprised conductive MoO_2 and metallic Ni (Fig. S4). Transmission electron microscopy (TEM) images of Int-Ni/MoO_2 suggested that the sharp-tip structure contained numerous nanopores with an average size of 3.52 nm (as determined by nitrogen adsorption-desorption measurements), which facilitated the mass transfer of the reactants and gas during electrocatalysis (Fig. S5a, b). In addition, the high-angle annular dark-field imaging-scanning transmission electron microscopy (HAADF-STEM) and energy-dispersive X-ray spectroscopy (EDX) results showed that the Ni nanoparticles were uniformly distributed on the MoO_2 substrate (Fig. S5c–e), confirming the heterostructure of Ni/MoO_2.

Notably, the prepared Int-Ni/MoO_2 exhibited high mechanical stability under ultrasonic treatment. A traditional rod-like NiMo/MoO_2 electrode was synthesised for comparison[22] (Figs. S6 and S7). As shown in Fig. 1b, the aqueous suspension of NiMo/MoO_2 turned black after 5 s of ultrasonication, indicating that the catalyst was shed from the NF

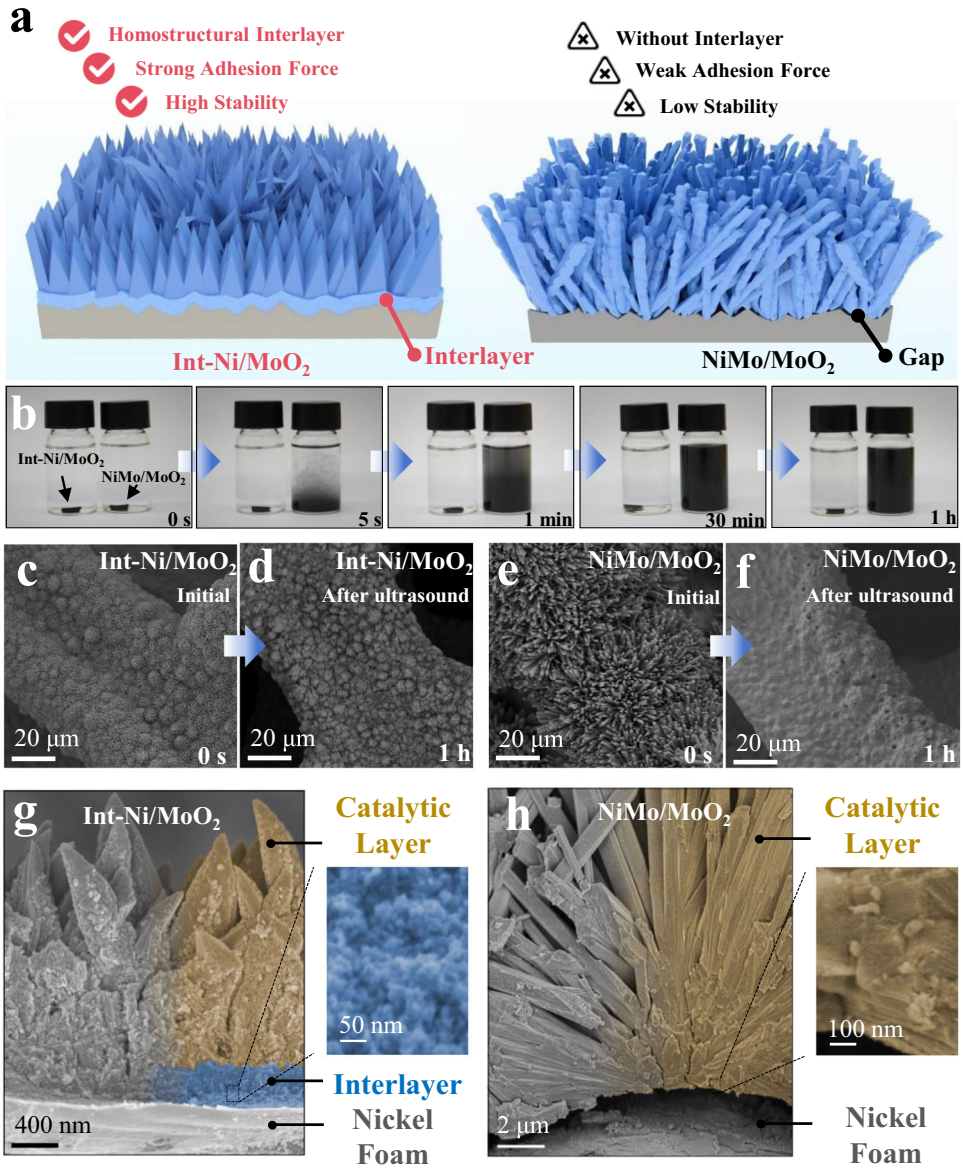

Fig. 1 | Characterisation of Int-Ni/MoO_2 electrode with an interlayer. **a** Schematic of enhanced stability of Int-Ni/MoO_2 with an interlayer. **b** Photos of ultrasonically treated (53 kHz) Int-Ni/MoO_2 (left) and NiMo/MoO_2 (right). **c**, **d** SEM images of Int-Ni/MoO_2 before (**c**) and after (**d**) ultrasonic treatment (53 kHz) for 1 h, respectively. **e**, **f** SEM images of NiMo/MoO_2 before (**e**) and after (**f**) ultrasonic treatment (53 kHz) for 1 h, respectively. **g** Cross-sectional SEM images of Int-Ni/MoO_2 with an interlayer. **h** Cross-sectional SEM images of NiMo/MoO_2 without an interlayer.

https://doi.org/10.1038/s41467-025-59933-6

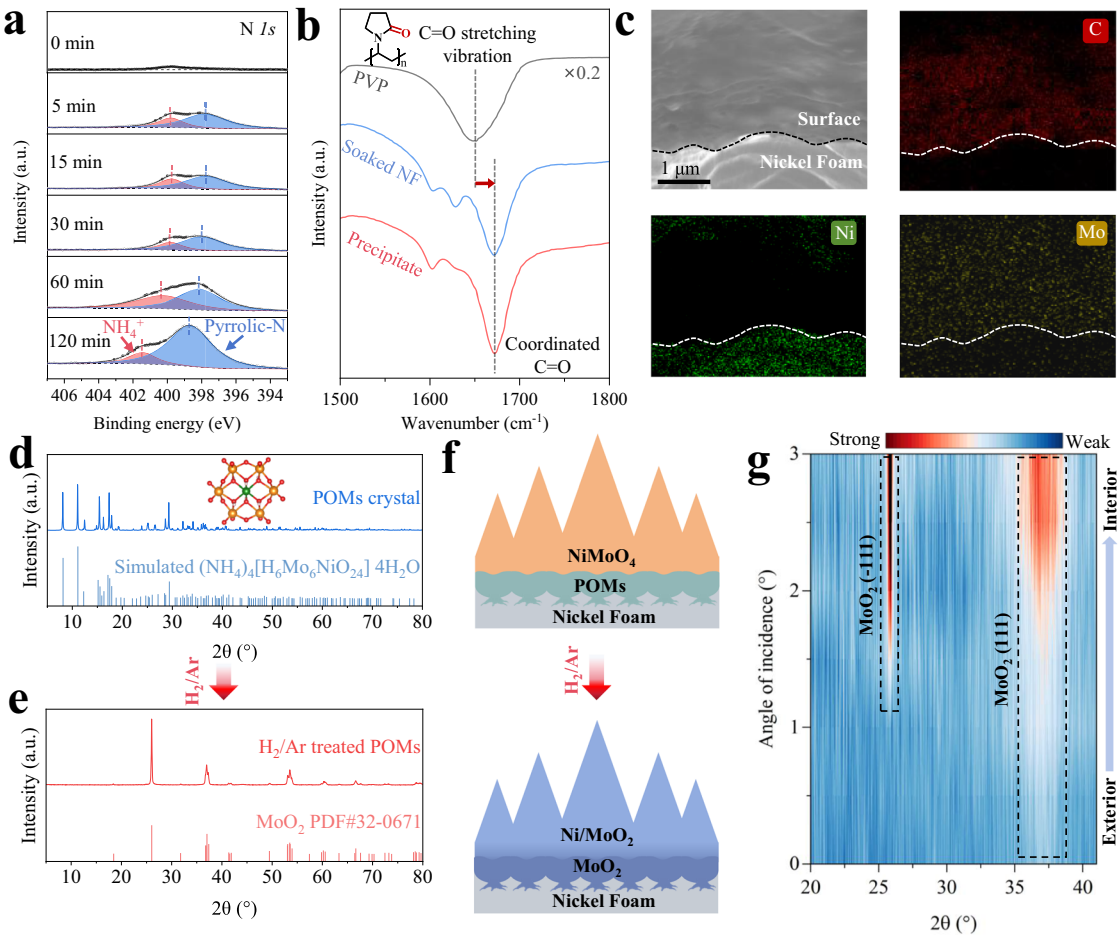

Fig. 2 | Characterisation of the homostructural interlayer in Int-Ni/MoO_2. **a** XPS spectra of the NF soaked in solutions of $(NH_4)_6Mo_7O_{24}$ and PVP with different soaking times. **b** FT-IR spectra of polyvinylpyrrolidone (PVP), precipitate, and soaked NF. **c** SEM-EDX images of soaked NF. **d**, **e** XRD patterns of precipitated crystals in solution and simulated $(NH_4)_4[H_6Mo_6NiO_{24}]$ $4H_2O$ (**d**); H_2/Ar-treated POMs and standard MoO_2 (**e**). **f** Schematic of the conversion of POM interlayer to a homostructural interlayer. **g** GIXRD patterns of Int-Ni/MoO_2.

substrate. In contrast, the solution with the Int-Ni/MoO_2 electrode showed negligible colour change even after an hour of ultrasonic treatment, confirming the high mechanical stability of the catalyst in Int-Ni/MoO_2 (Fig. S8). Moreover, the morphology of Int-Ni/MoO_2 was maintained after ultrasonic treatment, as confirmed by scanning electron microscopy (SEM) images (Fig. 1c, d and Fig. S9), while the NF substrate in NiMo/MoO_2 was completely exposed after ultrasonication (Fig. 1e, f and Fig. S10). The mass loss of Int-Ni/MoO_2 during ultrasonic treatment (53 kHz) was 7.5 ± 1.7%, significantly lower than that of NiMo/MoO_2 (69.9 ± 1.9% shown in Fig. S11). To explore the reason for the mechanical stability of Int-Ni/MoO_2, its brittle ruptured cross-sectional morphology was observed by SEM, where a sharp blade-shaped catalytic layer and a dense interlayer were observed on the surface of NF (Fig. 1g). However, for the NiMo/MoO_2 electrode, the rod-like catalyst was directly loaded onto the NF substrate without an interlayer (Fig. 1h). The dense interlayer in Int-Ni/MoO_2 is composed of nanoparticles measuring tens of nanometers, which act as a glue, attaching the catalytic layer tightly to the substrate and reinforcing the mechanical stability of the electrode (Fig. 1a), especially at high current densities with severe bubble strikes. The SEM-EDX results revealed that the elemental composition of the interlayer was identical to that of the catalytic layer, consisting of Mo, Ni, and O (Fig. S12).

The soaking process was further studied to examine the characteristics of the interlayer. During the soaking process, the colourless solution turned yellowish in the initial 5 min owing to the chemical etching of the NF by $Mo_7O_{24}^{6-}$, as evidenced by the presence of Ni^{2+} in the solution (Fig. S13a). As the soaking time increased, a green precipitate formed in the solution (Fig. S13b), and the SEM images showed that the rough surface of the NF became smoother, suggesting that the precipitate might attach to the NF surface (Fig. S14). The X-ray photoelectron spectra (XPS) of the NF revealed increased contents of pyrrolic-N (397.8 eV) and NH_4^+ (399.8 eV) after soaking (Fig. 2a). In addition, the peaks gradually shifted to higher binding energies, suggesting that PVP and NH_4^+ were coordinated to the metal or metal ions and deposited on the NF (Fig. S15). The blue shift of the C=O stretching vibration for the soaked NF in the Fourier transform infrared (FT-IR) spectra also confirmed that PVP was coordinated during the soaking process[23] (Fig. 2b). The SEM images of the soaked NF revealed that the surface contained C and Mo (Fig. 2c and Fig. S16). Moreover, the structure of the substance deposited on NF was identical to that of the precipitate in the solution (Fig. S17), and single-crystal XRD analysis confirmed it to be polyoxometalate (POM) $(NH_4)_4[H_6Mo_6NiO_{24}]$ $4H_2O$ (Fig. 2d and Fig. S18), which is similar to a previously reported structure[24] (Table S1). Based on the above results, the reactions of NF, $(NH_4)_6Mo_7O_{24}$, and PVP during soaking are proposed as follows. First, NF is corroded by $Mo_7O_{24}^{6-}$ to generate Ni^{2+} (Fig. S1). Then, Ni^{2+} and $Mo_7O_{24}^{6-}$ are restructured to form POMs with the assistance of the PVP ligand. Moreover, after the H_2/Ar treatment, the obtained POMs were converted to MoO_2 (Fig. 2e), which exhibited the same phase structure as the blade-shaped catalytic layer (Fig. 2f). This

https://doi.org/10.1038/s41467-025-59933-6

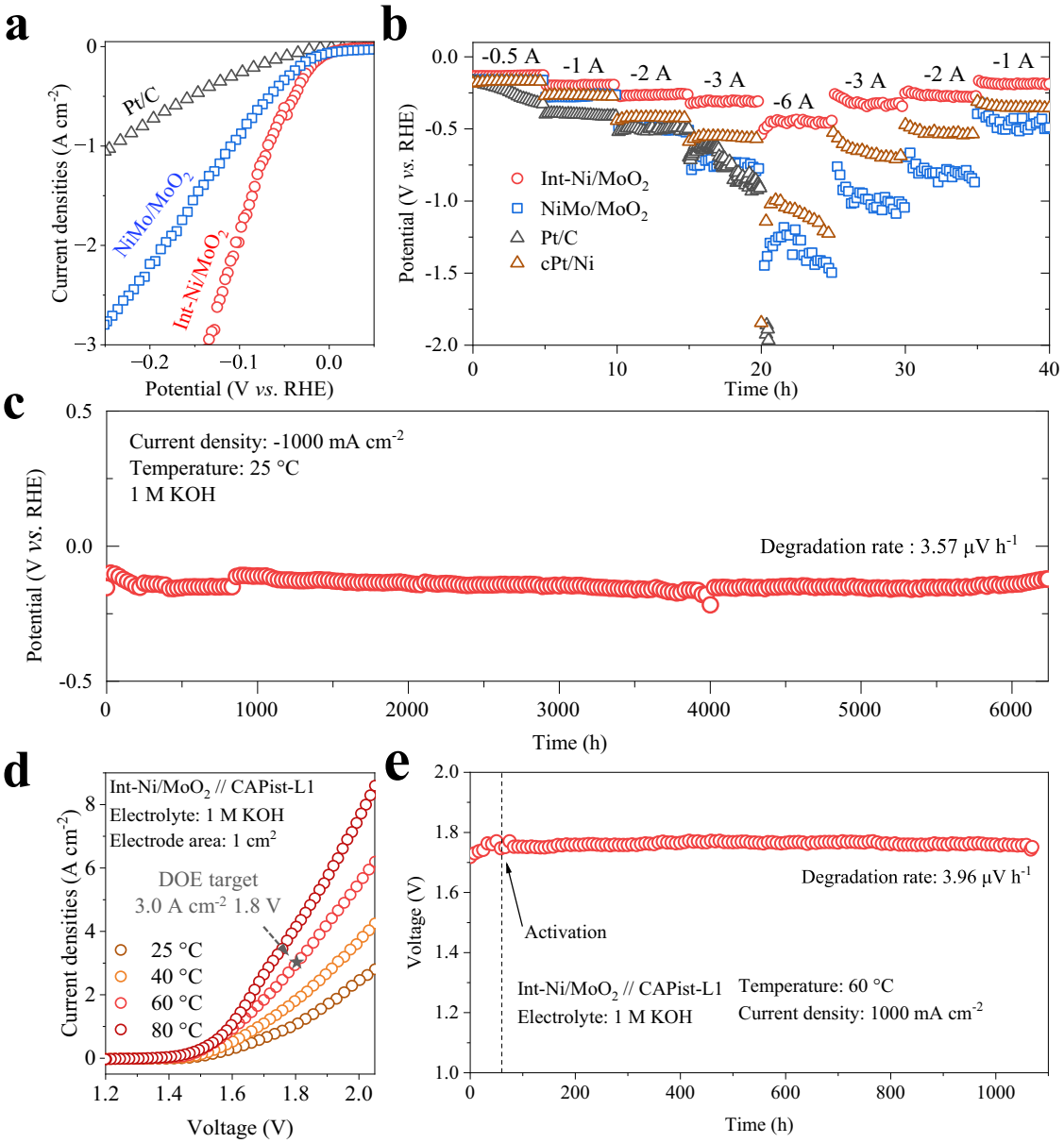

Fig. 3 | Catalytic activity and stability in 1 M KOH. a LSV curves of Int-Ni/MoO_2, NiMo/MoO_2, and Pt/C at scan rate of 5 mV s^{-1} without iR compensation. **b** Multiple current tests of Int-Ni/MoO_2, NiMo/MoO_2, Pt/C, and cPt/Ni (electrode area: 1 cm^2). **c** Long-term durability test of Int-Ni/MoO_2 at 25 °C. **d** LSV curves of the 1 cm^2 electrolyser at different temperatures at scan rate of 5 mV s^{-1}. **e** Stability measurement of the 1 cm^2 electrolyser at 60 °C under 1000 mA cm^{-2}. The degradation rate is calculated after 60 h activation.

homostructure allows the interlayer to act as a glue to stabilise the catalytic layer and transfer the bubble shock from the heterostructural interface (between the substrate and the catalytic layer) to the homostructural interface (between the interlayer and the catalytic layer), leading to high catalytic stability. Additionally, the grazing incidence X-ray diffraction (GIXRD) patterns of Int-Ni/MoO_2 revealed different crystalline structures in the interlayer and catalytic layer (Fig. 2g and Fig. S19). The exterior catalytic layer exhibited a broad peak at 36.8°, corresponding to the (111) plane of MoO_2. As the angle of incidence increased, a peak emerged 26.0°, which was attributed to the (−111) plane of MoO_2, confirming different crystallinities and orientations within the interlayer. The presence of a densely packed and highly crystalline interlayer is expected to improve mechanical stability during ultrasonic irradiation and enhance electrochemical stability at high current densities with intense mass transfer and gas collisions.

The HER activity was measured in 1 M KOH, with Hg/HgO as the reference electrode and a graphite plate as the counter electrode. As shown in Fig. 3a, Int-Ni/MoO_2 requires an overpotential of 46.4 ± 10.8 mV at −500 mA cm^{-2} (Fig. S20), which is lower than those of NiMo/MoO_2 (69.2 ± 4.9 mV) and Pt/C (154.0 ± 4.3 mV). Moreover, when the current density is increased to −1000 mA cm^{-2}, the overpotential for Int-Ni/MoO_2 only slightly increases to 73.2 ± 14.2 mV. The normalised HER performance also confirmed the high intrinsic activity of Int-Ni/MoO_2 (Fig. S21). Moreover, multicurrent tests were conducted on Int-Ni/MoO_2, NiMo/MoO_2, Pt/C, and commercial Pt on Ni (cPt/Ni) to evaluate their catalytic stability under harsh conditions (Fig. 3b). When the current density was increased to −6 A cm^{-2}, the overpotential of Pt/C sharply increased and exceeded the potential limit due to the weak adhesion strength of the binder. The NiMo/MoO_2 and cPt/Ni electrodes exhibited potential degradations of ~195 and 85 mV, respectively, when the current density returned to −1 A cm^{-2}, which was attributed to

catalyst detachment under harsh reaction conditions. However, Int-Ni/MoO_2 with a dense homostructural interlayer, exhibited negligible degradation. Short-term stability measurements confirmed the high catalytic stability of Int-Ni/MoO_2 (Fig. S22). SEM images of Int-Ni/MoO_2 before and after the HER (100 h at −1000 mA cm^{-2}) demonstrate that the blade-shaped structure is well preserved (Fig. S23). In contrast, the rod catalyst layer of NiMo/MoO_2 experienced extensive delamination after the HER at a high current density (Fig. S24). The XPS results indicated that Mo^0 in NiMo/MoO_2 was oxidised to a higher valence state during catalysis (Fig. S25). The enhanced mechanical stability of Int-Ni/MoO_2 ensured its high activity after ultrasonic treatment (Fig. S26). Int-Ni/MoO_2 also demonstrated better catalytic stability under current square-wave cycles than NiMo/MoO_2 in the accelerated stress test (Fig. S27)[25]. Furthermore, the catalytic activity of Int-Ni/MoO_2 did not show noticeable degradation after operating for more than 1000 h (Fig. 3c). Although the XRD and TEM results indicated that the structure of Int-Ni/MoO_2 after the HER became amorphous (Fig. S28a, b), its elemental composition and blade-shaped structure remained stable, as confirmed by the TEM-EDX and SEM results (Fig. S28c and S29). The faradaic efficiency (FE) of Int-Ni/MoO_2 was 100 ± 0.89% (Fig. S30). Owing to its unique sharp blade-shaped morphology and interlayer structure, the electrocatalytic performance and stability of Int-Ni/MoO_2 significantly surpass those of other reported catalysts at ampere-scale current densities (Fig. S31, Table S2 and S3).

The performance of Int-Ni/MoO_2 was further evaluated in an assembled AEM-WE cell in 1 M KOH. The previously reported NiFe-based anode (CAPist-L1)[4] and a commercial poly(aryl piperidinium) membrane (PAP-TP-85) were utilized in the cell. In 1 cm^2 (1 × 1 cm) AEM-WE device, this noble-metal-free cell only requires 1.79 V (at 25 °C) and 1.59 V (at 80 °C) to reach 1000 mA cm^{-2} (Fig. 3d). It achieves 7570 mA cm^{-2} at 2.0 V, showing a competitive performance with previously reported noble-metal-free AEM-WE devices (Table S4). The long-term durability of the Int-Ni/MoO_2-assembled cell is demonstrated for 1000 h at a cell voltage of ~1.7 V with a degradation rate of 3.96 μV h^{-1} (Fig. 3e). Moreover, the scale-up feasibility was evaluated using a 25 cm^2 (5 × 5 cm) AEM-WE device (Fig. S32). At 80 °C, the Int-Ni/MoO_2-assembled cell delivers a high current of 85.67 A (current density of 3430 mA cm^{-2}) at 1.8 V, exceeding the United States Department of Energy (DOE) 2026 target of 3000 mA cm^{-2} at 1.8 V for proton exchange membrane water electrolysis[26]. Notably, the voltage of the 25 cm^2 electrolyser was 1.58 V at 1000 mA cm^{-2}, which is similar that of the 1 cm^2 electrolyser (1.59 V). These results confirm the good scalability of Int-Ni/MoO_2-assembled cells for AEM-WE applications.

The chemical stability of the electrode was evaluated by monitoring the dissolution of metal ions during electrocatalysis. As shown in Fig. 4a, compared with Ni, a significantly higher amount of Mo was dissolved in both Int-Ni/MoO_2 and NiMo/MoO_2. This is attributed to the strong interactions between MoO_2 and alkali metals, which result in severe cathodic corrosion[27,28]. Additionally, the Int-Ni/MoO_2 electrode showed better chemical stability than NiMo/MoO_2, as indicated by the smaller amount of dissolved Mo (Fig. 4a), which is consistent with the XPS results (Figs. S33 and S34). The Ni/Mo atomic ratio on the exterior of the Int-Ni/MoO_2 electrode after catalysis was similar to that in the initial stage before the HER (Fig. 4b). However, the Ni/Mo atomic ratio of the catalytic NiMo/MoO_2 electrode was higher than the initial ratio, owing to the dissolution of Mo. Furthermore, after catalysis, the Ni/Mo atomic ratio within the interior of the NiMo/MoO_2 electrode was still higher than that of the initial electrode, implying that ion dissolution during catalysis was not restricted to the surface-active sites. Additionally, as shown in Fig. 4c, Int-NiMo/MoO_2 exhibits a stability number (S-number) of 1.7×10^5, which is significantly higher than that of NiMo/MoO_2 (4.9×10^4)[29]. Nanoindentation measurements of Int-Ni/MoO_2 indicated a maximum indentation depth (h_{max}) of 2050 ± 235 nm and a final depth (h_f) of 1277 ± 389 nm under a load of 2 mN, both significantly lower than the corresponding values of 2760 ± 364 nm (h_{max}) and 2591 ± 352 nm (h_f) for NiMo/MoO_2 (Fig. 4d and Fig. S35). This indicates that the hardness and compressive strength of the sharp blade-shaped Int-NiMo/MoO_2 with a dense interlayer are greater than those of the rod-like NiMo/MoO_2 without an interlayer. The nano-scratch measurements revealed that the critical binding forces of the catalyst layer on the substrate is 24.8 ± 3.1 mN for Int-NiMo/MoO_2 (Fig. S36a), which is higher than that of NiMo/MoO_2 (13.6 ± 3.1 mN). As a result, Int-Ni/MoO_2 maintains its structure and catalytic activity even when the current density reaches up to −6 A cm^{-2}. Gas contact angle measurements showed that the gas contact angle of Int-NiMo/MoO_2 was 147°, which is greater than that of NiMo/MoO_2 (124°) and Pt/C (89°). The low surface energy in Int-NiMo/MoO_2 at the gas/liquid interface facilitated bubble detachment, preventing overpotential fluctuations and releasing pressure shocks caused by bubble formation at ampere-scale current densities (Fig. 3b). The faster bubble evolution kinetics for Int-Ni/MoO_2 is confirmed by its smaller adhesive force (51.50 ± 1.09 μN), compared to 74.26 ± 1.53 μN for NiMo/MoO_2[30] (Fig. S36b). High-speed camera images revealed small dense bubbles on the surface of Int-Ni/MoO_2 when a potential was applied (Fig. 4f, g). However, unevenly distributed large bubbles were observed on NiMo/MoO_2 and Pt/C, as shown in both the top and side views. The average bubble diameter of 67.34 μm for the Int-Ni/MoO_2 electrode, compared to 119.27 μm for NiMo/MoO_2 and 146.32 μm for Pt/C (Figs. S37 and S38). Furthermore, no significant bubbles remained on the surface of the Int-Ni/MoO_2 electrode after the potential was removed (Fig. S37), indicating the low adhesive force of the bubbles on this electrode. The images of bubble growth and detachment were captured by a high-speed camera (Fig. S39). At −50 mA cm^{-2}, the average times for bubble detachment are 65 ± 14 ms, 175 ± 23 ms, and 457 ± 163 ms for the Int-Ni/MoO_2, NiMo/MoO_2, and Pt/C electrodes, respectively (Fig. S40). Therefore, the unique sharp blade-shaped structure and homostructural interlayer in Int-NiMo/MoO_2 enhanced its high mechanical stability and promoted smooth gas formation and detachment at ampere-scale current densities.

In summary, an Int-Ni/MoO_2 electrode with a homostructured interlayer was fabricated using a simple corrosion strategy. Int-Ni/MoO_2 exhibited significantly improved mechanical stability with higher critical binding forces compared to NiMo/MoO_2 without an interlayer. Moreover, the large gas contact angle and sharp blade shape of the catalytic layer in Int-Ni/MoO_2 allowed small bubbles to detach from the surface, enabling smooth mass transfer during intense electrocatalysis. Therefore, Int-Ni/MoO_2 exhibited a low overpotential of 73.2 ± 14.2 mV and long-term stability over 6000 h at −1000 mA cm^{-2} in 1 M KOH. The Int-Ni/MoO_2-assembled AEM-WE devices with areas of 1 cm^2 and 25 cm^2 further demonstrate their potential for industrialisation. Therefore, the corrosion and in situ growth strategies offer new methods to prepare ultrastable electrocatalysts with dense homostructural interlayers for HER and may inspire the synthesis of other electrocatalysts for various applications.

Methods

Chemicals

Ammonium molybdate [$(NH_4)_6Mo_7O_{24}$ $4H_2O$, Titan Industrial Co., ≥99.0%, Cas No. 12054-85-2], iron(II) sulfate ($FeSO_4 \cdot 7H_2O$, Aladdin Industrial, ≥99.0%, CAS No. 7782- 63-0), nickel(II) nitrate ($Ni(NO_3)_2 \cdot 6H_2O$, Aladdin Industrial, ≥99.0%, CAS No. 13478-00-7), ammonium fluoride [NH_4F, Sinopharm Chemical Reagent Co. Ltd., ≥96.0%, Cas No. 12125-01-8], polyvinylpyrrolidone [$(C_6H_9NO)_n$, Aladdin Industrial Co., K29-32, Cas No. 9003-39-8], platinum carbon [Pt/C, JM, 40%], commercial Pt on Ni (cPt/Ni, 2 μm Pt layer, Suzhou Shuer Tai Industrial Technology Co., Ltd.), isopropanol (i-PrOH, Sinopharm Chemical Reagent, ≥99.7%, CAS no. 67-63-0), ethanol [EtOH, Sinopharm Chemical Reagent Co. Ltd., ≥99.7%, Cas No. 64-17-5], acetone [CH_3COCH_3, Sinopharm Chemical Reagent Co. Ltd., ≥99.2%, Cas No. 67-64-1], potassium hydroxide [KOH, Macklin reagent, 95%, Cas No.

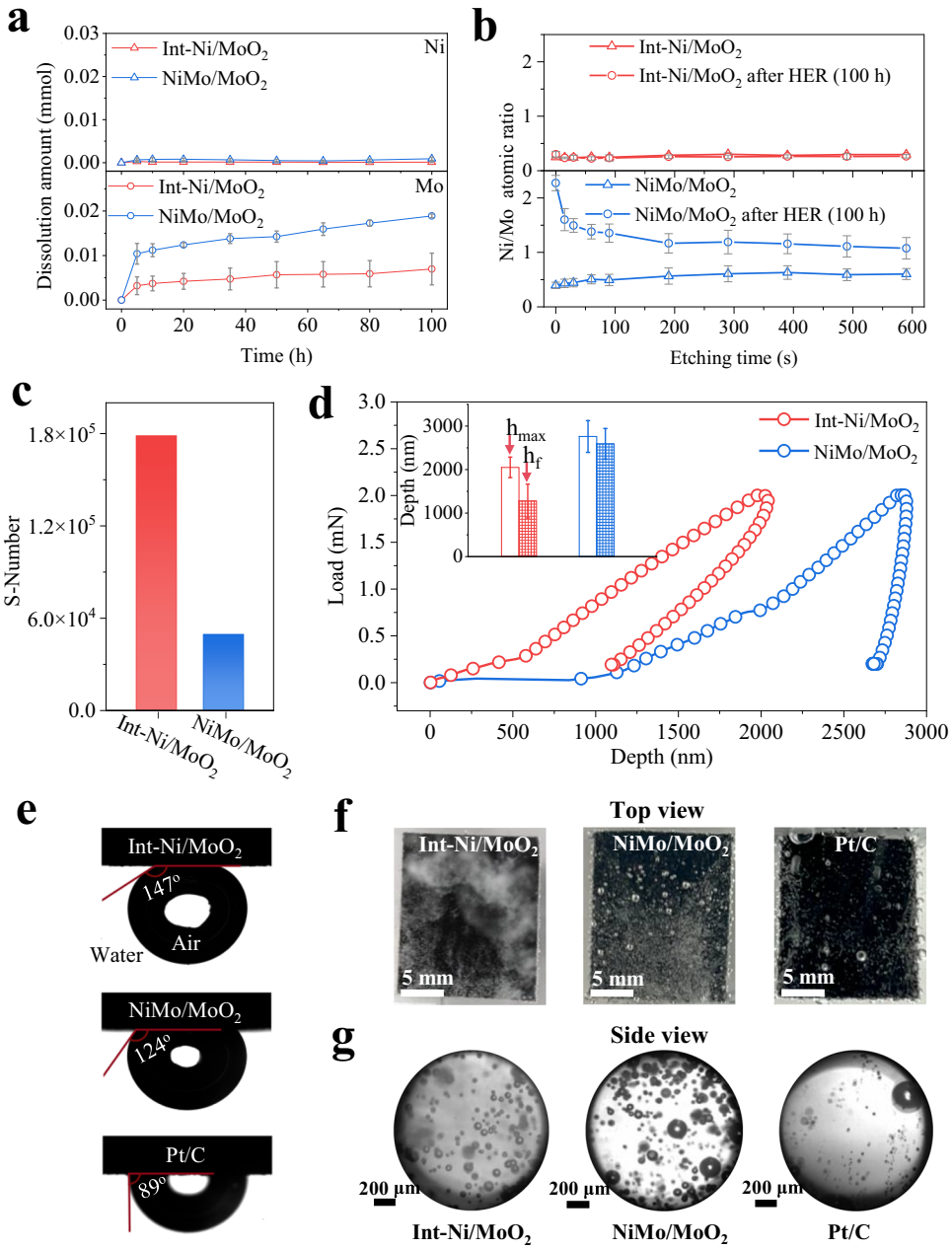

Fig. 4 | Stability mechanism for Int-Ni/MoO_2. **a** Data show mean values ± S.D. of three measurements metal dissolved amounts from Int-Ni/MoO_2 and NiMo/MoO_2 during short-term stability measurements at −500 mA cm^{-2}, as determined by ICP-MS. **b** Ni/Mo atomic ratio determined by XPS etching profiling for Int-Ni/MoO_2 and NiMo/MoO_2 before and after the HER test. Mean values ± S.D. were obtained by three independent measurements. **c** S-number results of Int-Ni/MoO_2 and NiMo/MoO_2 after 100 h of HER stability. **d** Load-displacement curves of Int-Ni/MoO_2 and NiMo/MoO_2. **e** Gas contact angles in water for Int-Ni/MoO_2, NiMo/MoO_2, and Pt/C. **f**, **g** Photographs of bubble attachment on Int-Ni/MoO_2, NiMo/MoO_2, and Pt/C at −50 mA cm^{-2} with the top view (**f**) and the side view (**g**).

1310-58-3], hydrochloric acid [HCl, Sinopharm Chemical Reagent Co. Ltd., 37%, Cas No. 7647-01-0] and Nafion 117 solution [Aladdin Industrial Co., 5.0% in EtOH, Cas No. 31175–20-9] were used without any pretreatment or purification. Ni foam [NF, Suzhou Jiashide Co. Ltd., ≥99.99%, thickness of 1.0 mm] was washed with 3 M HCl, EtOH, and acetone solutions to remove nickel oxide and hydrocarbons on the surface.

Catalyst preparation. Int-Ni/MoO_2

First, 1.00 g of $(NH_4)_6Mo_7O_{24}$ $4H_2O$, 0.10 g of polyvinylpyrrolidone, and 0.10 g of NH_4F were dissolved in 30 mL of deionised water to form a colourless solution. A pre-cleaned NF (1.5 × 2.5 cm) was soaked in the colourless solution and shaken at 25 °C for 2 h to form a white-green suspension. For the hydrothermal process, the suspension and NF were then transferred into a reactor and allowed to react at 150 °C for 6 h. The NF was then washed with deionised water and EtOH and dried in a vacuum oven at 25 °C for 12 h. The obtained precursor was then calcined at 500 °C for 2 h in a H_2/Ar (5:95) atmosphere to yield the Int-Ni/MoO_2. The loading masses of the catalyst and interlayer were 6.38 ± 0.37 mg cm^{-2} and 2.46 ± 0.15 mg cm^{-2}, respectively. The preparation method of the interlayer on nickel foam (I/NF) was the same as that of Int-Ni/MoO_2 but without the hydrothermal process.

NiMo/MoO_2[22]. A green-coloured solution was prepared by dissolving 0.44 g of $(NH_4)_6Mo_7O_{24}$ $4H_2O$ and 0.42 g of $Ni(NO_3)_2$ $6H_2O$ in 30 mL of deionised water. Then, a pre-cleaned NF (1.5 × 2.5 cm) was placed in the

green solution and reacted at 150 °C for 6 h. The NF was then washed with deionised water and EtOH and dried in a vacuum oven at 25 °C for 12 h. The obtained precursor was then calcined at 500 °C for 2 h in a H_2/Ar (5:95) atmosphere to yield NiMo/MoO_2. The loading mass of the catalyst was 33.5 ± 1.8 mg cm^{-2}.

Pt/C. First, 40 mg of Pt/C powder and 160 μL of a Nafion 117 solution (5.0% in EtOH) were added to the mixture of EtOH and i-PrOH (volume ratio of 1:1) under ultrasonication to form a uniform slurry. The as-prepared slurry was then sprayed evenly onto the NF using an N_2-borne spray gun, followed by thorough drying in a vacuum oven at 25 °C for 12 h. The Pt/C loading was controlled at 1.4 mg cm^{-2}.

CAPist-L1[4]. Two solutions were prepared by dissolving 1.45 g of $Ni(NO_3)_2{\cdot}6H_2O$ and 0.28 g of $FeSO_4{\cdot}7H_2O$ in 15 mL of i-PrOH and 5 mL of deionised water, respectively, and they were mixed under stirring to form a heterogeneous nucleation solution. NF (1.5 × 2.5 cm) was soaked in the above solution for 24 h at room temperature. The CAPist-L1 electrode was obtained by washing it with deionised water and EtOH and drying it in a vacuum oven at 25 °C. The loading mass of the catalyst was 3.8 ± 0.4 mg cm^{-2}.

Catalyst characterisation

X-ray diffraction (XRD, Bruker D8 advance) patterns were carried out on a Bruker powder diffractometer with Cu-K_α radiation. Grazing Incidence XRD (Bruker D8 discover) patterns were carried out on a Bruker powder diffractometer with Cu-K_α radiation. Scanning electron microscopy (SEM) was performed on a Zeiss Gemini 450 microscope system. High-resolution transmission electron microscopy (HRTEM) and energy-dispersive X-ray (EDX) analysis were carried out using a Thermo Fisher (Talos F200X G2) system at an acceleration voltage of 200 kV. An ESCALAB Xi+ analyser (Thermo Fisher) with Al radiation was employed for X-ray photoelectron spectroscopy (XPS) analysis, and the XPS depth profiling was performed using an Ar ion source. All XPS peaks were calibrated using the C *1s* line (284.8 eV) as the standard. Crystallographic data were collected on a Bruker D8 Venture diffractometer with Mo-Diamond K_α radiation (λ = 0.71073 Å) at 300 K. Unit cell determination and data reduction were processed using the APEX3 programme. The crystal structure was solved and refined by direct methods with SHELXT and SHELXL programs[31,32]. Load-displacement curves were obtained by nanoindentation measurements on a Nano Test Vantage with a maximum load of 2 mN. Nano-scratch measurement were carried out on the Nano Indenter G200X with maximum load of 50 mN and displacement of 200 μm. The catalyst growth on the nickel foil were used for the nano-scratch measurement. Inductively coupled plasma mass spectrometry (ICP-MS, iCAP RQ) was performed using a Thermo Fisher inductively coupled plasma mass spectrometer. A high-speed camera (ACS-1 M60) was used to capture photos of bubble attachment over catalysts at 50 mA cm^{-2}. Fourier-transform infrared (FTIR, Nicolet iS50) spectra were obtained using a Thermo Fisher FTIR microspectrometer. Ultrasonic measurements were conducted using an ultrasonic cleaner (KUDOS, SK2200H) operating at frequencies of 53 and 35 kHz. The Int-NiMo/MoO_2 powder was collected after ultrasonically treating the Int-NiMo/MoO_2 electrode with EtOH in an ice water bath for several minutes. The suspension containing the peeled catalyst was dropped on a single-crystal silicon sample holder, a carbon conductive tape, and a lacey carbon-supported copper grid for the XRD, XPS, and TEM analyses, respectively. The error bars represent the standard deviation calculated from the measurements of three independently prepared electrodes.

Electrochemical measurements

The electrochemical HER activity and stability were measured on an Autolab Vionic workstation using a typical three-electrode system in 1 M KOH (59.05 g KOH in 100 mL H_2O, pH = 13.78 ± 0.11) without IR compensation. The error bars in the electrochemical measurements represent the standard deviations calculated from the measurements of three independently prepared electrodes. The measurements were performed in a glass cell (Tianjin Hengsheng Ida C002, 150 mL) with an electrolyte volume of 80 mL. The glass cell was washed with 0.1 M HCl, deionised water, and EtOH separately before use. Hg/HgO (calibrated to 0.930 V in 1 M KOH using a standard hydrogen electrode) was used as the reference electrode, and graphite was used as the counter electrode. The working electrode was cut into an L-type shape with an immersion area of 1.0 × 1.0 cm during the test. The distance between the working and reference electrodes was maintained at 1–2 mm. Linear sweep voltammetry (LSV) measurements were performed at a scan rate of 5 mV s^{-1}. Electrochemical impedance spectroscopy was tested at an open circuit voltage with an AC amplitude of 5 mV. Solution resistances in 1 M KOH are 0.041 ± 0.004, 0.052 ± 0.009 and 0.089 ± 0.005 Ω for Int-Ni/MoO_2, NiMo/MoO_2, and Pt/C, respectively. In the multiple-current tests, online water injection was employed to maintain a constant KOH level. In the long-term durability test at −1000 mA cm^{-2}, the counter electrode was substituted with a nickel mesh due to the instability of graphite. The electrolyte temperature may be slightly higher than 25 °C under high current densities. The degradation rate (r) was calculated as follows:

$$r = \frac{\eta_f - \eta_i}{t} \quad (1)$$

where η_f is the final overpotential or voltage (V), η_i is the initial overpotential or voltage (V), and t is the catalysis time (h).

The 1 cm^2 and 25 cm^2 AEM-WEs were measured in 1 M KOH on the Autolab PGSTAT302 (with 20 A booster) and Solartron Analytical (with 100 A booster) workstation, respectively. NiFe-based anode (CAPist-L1) and commercial poly(aryl piperidinium) membrane (PAP-TP-85) were utilized in the cell. The membrane was soaked in 1 M KOH for 6 h before used. LSV measurements were performed at a scan rate of 10 mV s^{-1}. The stability tests were measured at 1000 mA cm^{-2} with the online water injection to maintain a constant KOH level.

Turnover frequency (TOF)

The TOF was calculated using the following equation[33,34]:

$$TOF = \frac{j \times N_A}{2 \times F \times (n_{Mo} + n_{Ni})} \quad (2)$$

where j is the current (A), N_A is the Avogadro's constant, F is the Faraday constant, and $n_{Mo} + n_{Ni}$ represents the total number of reactive sites. n_{Mo} and n_{Ni} were determined based on the XPS results, assuming that the metal atoms on the surface are the active centres and are all accessible to the electrolyte.

Accelerated stress testing

Accelerated stress testing was carried out by square-wave cycles between a low current density of 0 mA cm^{-2} and a high current density of −1000 mA cm^{-2}. The current density was held for 2 s per cycle. LSV measurements were performed every 5000 cycles.

Faradaic efficiency (FE)

FE is defined as the ratio of the experimentally determined hydrogen amount to the theoretically expected amount. Hydrogen gas was collected by displacing the water. A constant potential was applied to the electrode, and the volume of the generated gas was recorded. Each experiment was conducted in triplicate, and the FE was calculated

using the following equation:

$$FE(\%) = \frac{\frac{V}{24.5} \times 2 \times F}{Q} \times 100\,\% \quad (3)$$

where V (L) is the volume of generated H2, F is the Faraday constant, and Q is the quantity of the applied charge.

Stability number

The stability number was calculated by the following equation[29]:

$$S_{Number} = \frac{n_{H_2(HER)}}{n_{Mo(dissolved)}} \quad (4)$$

where $n_{H_2(HER)}$ is the amount of generated H_2 per unit time, and n_{Mo} is the amount of dissolved Mo per unit time obtained by ICP-MS.

Data availability

All data supporting this study are available within this article and its Supplementary Information. Any additional relevant data are available upon request. Source data are provided in this paper. Source data are provided with this paper.

References

1. Xie, H. et al. A membrane-based seawater electrolyser for hydrogen generation. *Nature* **612**, 673–678 (2022).
2. Wan, C. et al. Amorphous nickel hydroxide shell tailors local chemical environment on platinum surface for alkaline hydrogen evolution reaction. *Nat. Mater.* **22**, 1022–1029 (2023).
3. Zhu, J., Hu, L., Zhao, P., Lee, L. Y. S. & Wong, K.-Y. Recent advances in electrocatalytic hydrogen evolution using nanoparticles. *Chem. Rev.* **120**, 851–918 (2020).
4. Li, Z. H. et al. Seed-assisted formation of NiFe anode catalysts for anion exchange membrane water electrolysis at industrial-scale current density. *Nat. Catal.* **7**, 944–952 (2024).
5. Zhang, C. et al. Superaerophilic/superaerophobic cooperative electrode for efficient hydrogen evolution reaction via enhanced mass transfer. *Sci. Adv.* **9**, eadd6978 (2023).
6. Jin, M. et al. Strategies for designing high-performance hydrogen evolution reaction electrocatalysts at large current densities above 1000 mA cm^{-2}. *ACS Nano* **16**, 11577–11597 (2022).
7. Xu, X. et al. Highly efficient all-3D-printed electrolyzer toward ultrastable water electrolysis. *Nano Lett.* **23**, 629–636 (2023).
8. Angulo, A., van der Linde, P., Gardeniers, H., Modestino, M. & Fernández Rivas, D. Influence of bubbles on the energy conversion efficiency of electrochemical reactors. *Joule* **4**, 555–579 (2020).
9. Yu, J. et al. Interfacial nanobubbles' growth at the initial stage of electrocatalytic hydrogen evolution. *Energy Environ. Sci.* **16**, 2068–2079 (2023).
10. Kim, J. et al. Efficient alkaline hydrogen evolution reaction using superaerophobic ni nanoarrays with accelerated H_2 bubble release. *Adv. Mater.* **35**, 2305844 (2023).
11. Park, S. et al. Solutal Marangoni effect determines bubble dynamics during electrocatalytic hydrogen evolution. *Nat. Chem.* **15**, 1532–1540 (2023).
12. Wang, J. et al. Dynamically adaptive bubbling for upgrading oxygen evolution reaction using lamellar fern-like alloy aerogel self-standing electrodes. *Adv. Mater.* **36**, 2307925 (2024).
13. Li, D. et al. Highly quaternized polystyrene ionomers for high performance anion exchange membrane water electrolysers. *Nat. Energy* **5**, 378–385 (2020).
14. Chen, N., Jiang, Q., Song, F. & Hu, X. Robust piperidinium-enriched polystyrene ionomers for anion exchange membrane fuel cells and water electrolyzers. *ACS Energy Lett.* **8**, 4043–4051 (2023).
15. Zuo, Y. et al. Ru–Cu Nanoheterostructures for efficient hydrogen evolution reaction in alkaline water electrolyzers. *J. Am. Chem. Soc.* **145**, 21419–21431 (2023).
16. Wang, X. et al. Rationally modulating the functions of Ni_3Sn_2-$NiSnO_x$ nisnox nanocomposite electrocatalysts towards enhanced hydrogen evolution reaction. *Angew. Chem.* **135**, e202301562 (2023).
17. Huang, L. et al. Ion irradiation activated catalytic activity of $MoSe_2$ nanosheet for high-efficiency hydrogen evolution reaction. *Adv. Energy Mater.* **13**, 2300651 (2023).
18. Shi, X. et al. Hierarchical crystalline/amorphous heterostructure $MoNiO_x$ for for electrochemical hydrogen evolution with industry-level activity and stability. *Adv. Funct. Mater.* **33**, 2307109 (2023).
19. Mu, X. et al. Breaking the symmetry of single-atom catalysts enables an extremely low energy barrier and high stability for large-current-density water splitting. *Energy Environ. Sci.* **15**, 4048–4057 (2022).
20. Liu, H. et al. Dual interfacial engineering of a Chevrel phase electrode material for stable hydrogen evolution at 2500 mA cm^{-2}. *Nat. Commun.* **13**, 6382 (2022).
21. Qiao, M. et al. Design strategies towards advanced hydrogen evolution reaction electrocatalysts at large current densities. *Chem. Eur. J.* **30**, e202303826 (2024).
22. Zhang, J. et al. Efficient hydrogen production on $MoNi_4$ electrocatalysts with fast water dissociation kinetics. *Nat. Commun.* **8**, 15437 (2017).
23. Baykal, A. et al. Polyol synthesis of (polyvinylpyrrolidone) PVP–Mn_3O_4 nanocomposite. *J. Alloy. Compd.* **502**, 199–205 (2010).
24. Lee, U., Joo, H.-C. & Kwon, J.-S. Tetraammonium hexahydrogen hexamolybdonickelate(II) tetrahydrate, $(NH_4)_4[H_6NiMo/MoO_{26}O_{24}].4H_2O$. *Acta Crystallogr. Sect. E* **58**, i6–i8 (2002).
25. Spöri, C., Brand, C., Kroschel, M. & Strasser, P. Accelerated degradation protocols for iridium-based oxygen evolving catalysts in water splitting devices. *J. Electrochem. Soc.* **168**, 034508 (2021).
26. Shi, W. et al. Ultrastable supported oxygen evolution electrocatalyst formed by ripening-induced embedding. *Science* **387**, 791–796 (2025).
27. Hersbach, T. J. P., Yanson, A. I. & Koper, M. T. M. Anisotropic etching of platinum electrodes at the onset of cathodic corrosion. *Nat. Commun.* **7**, 12653 (2016).
28. Hersbach, T. J. P. et al. Alkali metal cation effects in structuring Pt, Rh, and Au surfaces through cathodic corrosion. *ACS Appl. Mater. Inter.* **10**, 39363–39379 (2018).
29. Geiger, S. et al. The stability number as a metric for electrocatalyst stability benchmarking. *Nat. Catal.* **1**, 508–515 (2018).
30. Lu, Z. et al. Ultrahigh hydrogen evolution performance of under-water "superaerophobic" MoS2 nanostructured electrodes. *Adv. Mater.* **26**, 2683–2687 (2014).
31. Sheldrick, G. A short history of SHELX. *Acta Crystallogr. Sect. A* **64**, 112–122 (2008).
32. Zhao, H. & Schuck, P. Combining biophysical methods for the analysis of protein complex stoichiometry and affinity in SEDPHAT. *Acta Crystallogr. Sect. D.* **71**, 3–14 (2015).
33. Li, Y. et al. MoS_2 nanoparticles grown on graphene: an advanced catalyst for the hydrogen evolution reaction. *J. Am. Chem. Soc.* **133**, 7296–7299 (2011).
34. Kibsgaard, J., Jaramillo, T. F. & Besenbacher, F. Building an appropriate active-site motif into a hydrogen-evolution catalyst with thiomolybdate $[Mo_3S_{13}]^{2-}$ clusters. *Nat. Chem.* **6**, 248–253 (2014).

Acknowledgements

This work was financially supported by the National Key R&D Program of China (2022YFA0911902), the National Natural Science Foundation of China (22088102, 22301248), the Research Center for Industries of the Future (RCIF) at Westlake University, China Postdoctoral Science Foundation (2022M712837, 2023M733175). The authors would like to thank

Dr. Wenxing Yang and Qiliang Liu at the Center of Artificial Photosynthesis for Solar Fuels and the Department of Chemistry at Westlake University for their help in high-speed camera measurement.

Author contributions

Conceptualization and methodology: L. Sun – synthesis, characterization, and test: A. Dong, G. Lin, Z. Li, W. Wu, X. Cao, W. Li, L. Wang, Y. Zhao and D. Chen. Data analysis: A. Dong and G. Lin. Writing – original draft: A. Dong and G. Lin. Writing – review and editing: G. Lin and L. Sun.

Competing interests

The authors declare no competing interests.

Additional information

Supplementary information The online version contains supplementary material available at https://doi.org/10.1038/s41467-025-59933-6.

Correspondence and requests for materials should be addressed to Licheng Sun.

Peer review information *Nature Communications* thanks the anonymous reviewer(s) for their contribution to the peer review of this work. A peer review file is available.